Shallow Seismicity in the Long Beach–Seal Beach, California Area

Yan Yang*[1] and Robert W. Clayton[1]

Abstract

Seismicity can help to locate fault zones that are often difficult to characterize in densely populated urban areas. In this study, we use three dense nodal arrays consisting of thousands of sensors to detect and locate seismic events in the Long Beach–Seal Beach area of California. Small events can be detected at sufficient signal-to-noise levels during the night, when urban noise is relatively low. We detect and locate >1000 events with M_L below 2. Most of the located events are clustered at very shallow depth (0–2 km). The results support previous suggestions that the shallow Newport-Inglewood fault is a wide splayed fault in this area. The seismicity pattern also compares well with some newly identified faults from reflection seismic surveys. The shallow events, which elude detection by the regional seismic network, underscore the complex nature of the faults and their seismic hazard.

Cite this article as Yang, Y., and R. W. Clayton (2023). Shallow Seismicity in the Long Beach–Seal Beach, California Area, *Seismol. Res. Lett.* **XX**, 1–9, doi: 10.1785/0220220358.

Supplemental Material

Introduction

According to modern assessment (e.g., Field *et al.*, 2015), seismic hazard in the Los Angeles and the Long Beach area, California, is largely controlled by the Newport-Inglewood fault (NIF; Taber, 1920). Several studies have concluded that the damaging 1933 Long Beach earthquake (Wood *et al.*, 1933) occurred on the NIF, rupturing from southeast to northwest (Hauksson and Gross, 1991; Hough and Graves, 2020), with the significant damage concentrated in the Long Beach and south Los Angeles areas (Wood *et al.*, 1933; Hough and Graves, 2020). The NIF is predominantly a strike-slip fault with an estimated 60 km cumulative offset, but it does not have significant seismicity associated with it (Hauksson, 1987). There are a large number of major oil fields along the NIF (Eaton, 1933), and cross sections derived as part of hydrocarbon exploration show that the NIF starts to splay at depths shallower than 5 km (Gish and Boljen, 2021). Detailed characterization of hazard in this densely populated urban area has been hindered by the paucity of modern seismicity and the complexity of shallow fault structures.

The current Southern California Seismic Network (SCSN) catalog has located a total of 546 events from 1932 to 2008 with a nominal magnitude of completeness of $M_c > 1.8$ (Hutton *et al.*, 2010) and a total of 199 events from 2008 to 2018 using template matching methods with a nominal magnitude of completeness of $M_c > 0.3$ (Ross *et al.*, 2019, Fig. 1). This zone is also unusual for southern California in that it has a number of deep events (below 15 km). There have been 49 such events in the SCSN catalog in the past 20 yr. Some of these events are actually below the Moho, according to studies by Inbal *et al.* (2015, 2016) using part of the same arrays' data used in this study. Detecting and locating these deep events required preprocessing to reduce the surface noise, which consisted of downward continuation of the recorded wavefield to a depth of 5 km (Inbal *et al.*, 2016). This brings the deep events closer to the array and reduces the surface noise (primarily surface waves) considerably. This was confirmed by Yang *et al.* (2021), who showed that the deep events are not evident with standard processing. The downward continuation step precludes detection of earthquakes shallower than 5 km depth. In this study, we develop methodology to detect and locate shallow events.

The paucity of cataloged seismicity may be due to the sparse SCSN network (interstation spacing of 10 km or ~0.01 stations/km^2) in the Long Beach area. In this study, we use three temporary, dense-array surveys deployed in the area for oil exploration (Fig. 1). These arrays comprise short-period vertical sensors that have a spatial density of ~100 sensors/km^2, which facilitates the detection of small local earthquakes. The study area is, however, a very noisy urban region, and this makes it a challenge to detect weak seismicity. In this article, we exploit the density of the array to detect the coherent signals of the shallow seismicity. Modern methods such as template matching (Shelly *et al.*, 2007; Ross *et al.*, 2019) and machine learning approaches (Ross *et al.*, 2018; Zhu and Beroza, 2019; Mousavi *et al.*, 2020) cannot be used

1. Seismological Laboratory, California Institute of Technology, Pasadena, California, U.S.A., https://orcid.org/0000-0002-6105-2918 (YY); https://orcid.org/0000-0003-3323-3508 (RWC)

*Corresponding author: yanyang@caltech.edu

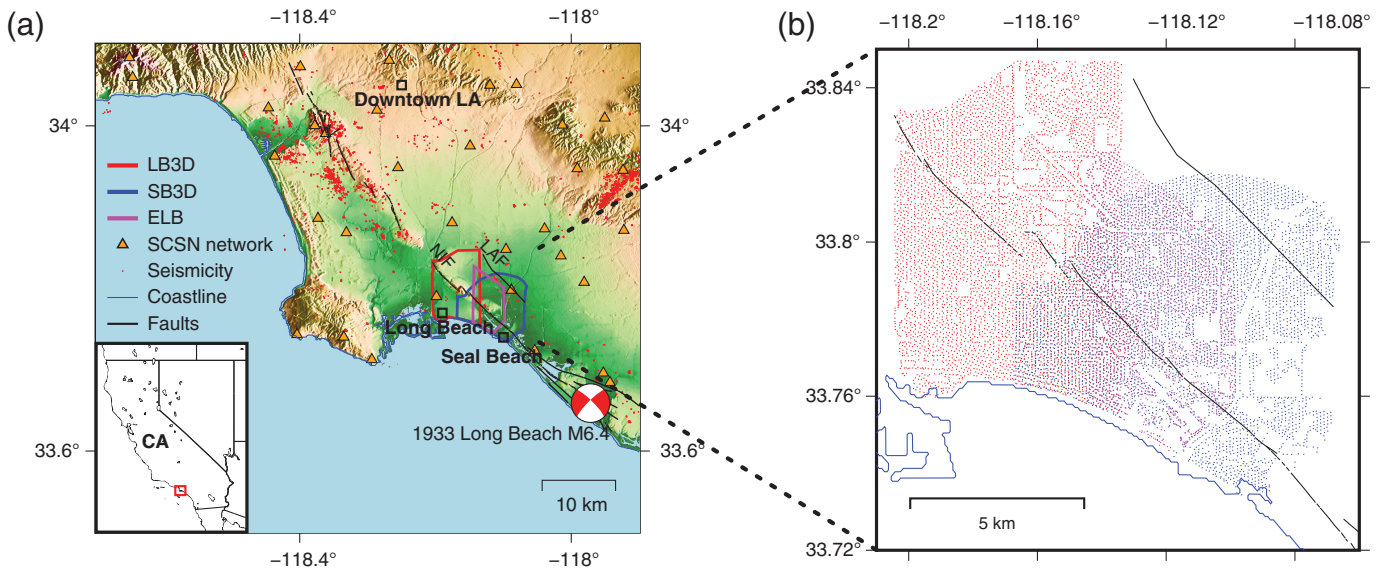

Figure 1. (a) Map of the study area. The lower left inset map shows the location of the study area within California. The red dots show seismicity from the template matching–based catalog (Ross *et al.*, 2019), the focal mechanism plot is the focal mechanism for the 1933 **M** 6.4 Long Beach earthquake (Hauksson and Gross, 1991), and the black lines are the known faults from the U.S. Geological Survey (USGS) Quaternary Fault and Fold Database. The orange triangles represent the Southern California Seismic Network (SCSN) stations. The red, blue, and magenta lines outline the Long Beach (LB3D), Seal Beach (SB3D), and extended Long Beach (ELB) arrays, respectively. (b) The zoomed-in view of the three nodal arrays is shown on the right, with dots showing the location of the sensors. LA, Los Angeles; LAF, Los Alamitos fault; NIF, Newport-Inglewood fault.

directly because of the lack of templates or a training set for the nodal arrays and the seismicity in this area. Therefore, we use a standard short-term average/long-term average (STA/LTA) method and a spatial clustering filter to exploit station density. One of the challenges of this study is that shallow detection is often associated with anthropological activities; therefore, we focus on the nighttime events, when the urban area is considerably quieter seismically, as shown in Figure 2.

Data and Methods

Data used in this study come from three separate surveys that occurred at different times and were deployed for different lengths of time. The survey information is shown in Table 1. The arrays have an average sensor spacing of ∼100 m. The instruments are Fairfield Z-land nodes each consisting of a vertical short-period velocity sensor with a lower-frequency corner of 10 Hz. Previous studies with these data have shown that these instruments have sensitivity to frequencies as low as ∼0.1 Hz (Lin *et al.*, 2013; Castellanos *et al.*, 2020). The data were recorded continuously at 500 Hz sampling rates and were then downsampled to 250 Hz.

The Long Beach–Seal Beach study area has a high level of cultural noise that varies significantly over the span of a day. Figure 2 shows the hourly root mean square (rms) energy averaged over the stations of the Seal Beach array and the duration of the survey. There is a factor of approximately two difference in noise levels between daytime and nighttime hours. Because the focus of our study is on elucidation of shallow fault structures rather than catalog completeness, we restrict our analysis to nighttime hours (9 p.m. to 5 a.m. Pacific time) to maximize the signal-to-noise ratio. We excluded Sunday nights from the analysis with the Long Beach array because the seismic-survey contractor used this time period to run the vibrator sources at full power near the Long Beach airport. The band-pass filter of 2–8 Hz is designed to remove the vibrator sweep frequencies, which is 8–80 Hz. In normal operations, the vibrators are only operated during the daytime at highly reduced power (Snover *et al.*, 2020). Some machine learning denoisers are proposed recently to remove the urban noise (Yang *et al.*, 2022), but these methods are based on trace-by-trace method and may degrade the spatial correlated pattern of the earthquakes recorded in a dense nodal array (Fig. S1, available in the supplemental material to this article).

In this study, the *P* waves are picked with an STA/LTA-based picker (Bungum *et al.*, 1971; Withers *et al.*, 1998; White *et al.*, 2019). The window lengths of 0.25 and 10.0 s are used for the STA and LTA, respectively. The STA/LTA algorithm registers a detection when the ratio of the two averages (each calculated as the rms signal amplitude) exceeds an onset threshold of 5 and remains above a secondary threshold of 2 for at least 2 s.

The second step is to associate the single station-based picks into events. The STA/LTA method can be triggered by spurious signals that originate from shallow noise sources in the vicinity of the geophones. Therefore, we associate the picks in both time and space to mitigate the false detections. It takes

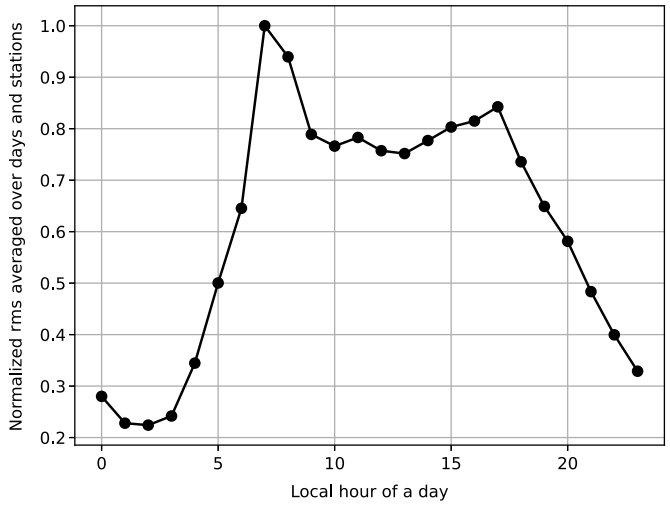

Figure 2. The noise amplitude variation with local hours. The curve is averaged over all the nodes in the SB3D array and for all the dates, which clearly reveals day–night anthropogenic noise variation and rush hours. rms, root mean square.

a maximum of 2 s for *P* waves to traverse the arrays, and hence, a quick way to associate events is to count the number of single-station picks within a 2 s sliding window. If, at any moment, the number of picks is larger than two standard deviations from the mean of a day, a potential event is declared (Fig. 3).

After the association, candidate events are further screened by a spatial coherence filter. The local anthropogenic noise may trigger nearby sensors but not usually the sensors away from the triggered one. For a pick at sensor to be kept in the associated event, we require that 20% of sensors within 1 km of that sensor to also have picks (Fig. 3f). After the spatial clustering, the number of events decreases from >600,000 to ∼50,000. This process eliminates most of the uncorrelated random picks.

Identified events are located by a cascade of methods designed to improve locations. For the initial location, the events are individually located using the algorithm NonLinLoc (Lomax *et al.*, 2000, 2014), which is a probabilistic, global-search approach. During the grid search, it is assumed that both the velocity model and picks can produce 0.5 s errors. This input prior uncertainty is quite large and could be improved using a path-dependent error. After this, a double-difference relocation is performed to refine the relative location. The differential times of all the event pairs are calculated with cross correlation of the waveforms in a window around the *P*-wave arrival times (0.5 s before and 2 s after). The differential travel times obtained by cross-correlating waveforms are input into GrowClust (Trugman and Shearer, 2017), which is a cluster-based double-difference relocation algorithm. A minimum of eight differential travel times and a minimum cross-correlation coefficient of 0.7 are required to relocate each event pair. For both absolute and relative location, a 1D velocity model averaged from the Southern California Earthquake Center Community Velocity Models (SCEC-CVMs) in this region is used (Small *et al.*, 2017). The event is kept if either is relocated by GrowClust or has an uncertainty (estimated by NonLinLoc) <2 km. After relocation, the number of events decreases from 50,000 to 3363 (including day and night). We use bootstrapping to estimate the error of the relocation results (Trugman and Shearer, 2017). The resulted average horizontal error is 0.12 km, and the average vertical error is 0.16 km.

TABLE 1
General Information about the Three Arrays

ID	Date (yyyy/mm/dd–yyyy/mm/dd)	Number of Nodes	Name
LB3D	2011/01/05–2011/06/15	5441	Long Beach
ELB	2012/01/10–2012/04/13	2484	East Long Beach
SB3D	2018/01/22–2018/02/15 (span of complete array)	5228	Seal Beach

ELB, extended Long Beach; LB3D, Long Beach; SB3D, Seal Beach.

The local magnitude of the events can be estimated with a simple regression based on the largest amplitudes and hypocentral distances recorded at the sensors as used in a Wood–Anderson seismograph (Richter, 1935):

$$M_L = \log_{10} A + a \log_{10} \Delta + b, \quad (1)$$

in which A is the peak amplitude of the *P*-wave waveform recorded at a station with epicentral distance Δ. For calibration, we use a total of 11 events that are already recorded in the SCSN catalog and are located closest to the nodal array. Given the accurate magnitudes M_L from the SCSN catalog and the peak amplitudes A and the epicentral distances Δ based on the recordings of our nodes, we can optimize the empirical parameters a and b in the equation with linear regression. We have the resulted best-fitted a = 0.4958 and b = 1.8517. With the fixed parameters a and b, we calculate the magnitude for the events that are not in the SCSN catalog but detected and located by the nodal arrays. For each event, we determine its magnitude using the median of the magnitudes calculated by all the nodes following equation (1).

Results

The nearby SCSN cataloged events are all detected and located with better-resolved hypocenters (Fig. 4). They are not, however, included in our relocated catalog because they are outside the array area, and the relocation requires multiple events with coherent waveforms. The SCSN cataloged events are relatively large (M_w ∼2) and do not have repeating counterparts within several months. We detected, located, and relocated a total of 1262 nighttime events during a noncontinuous period of eight

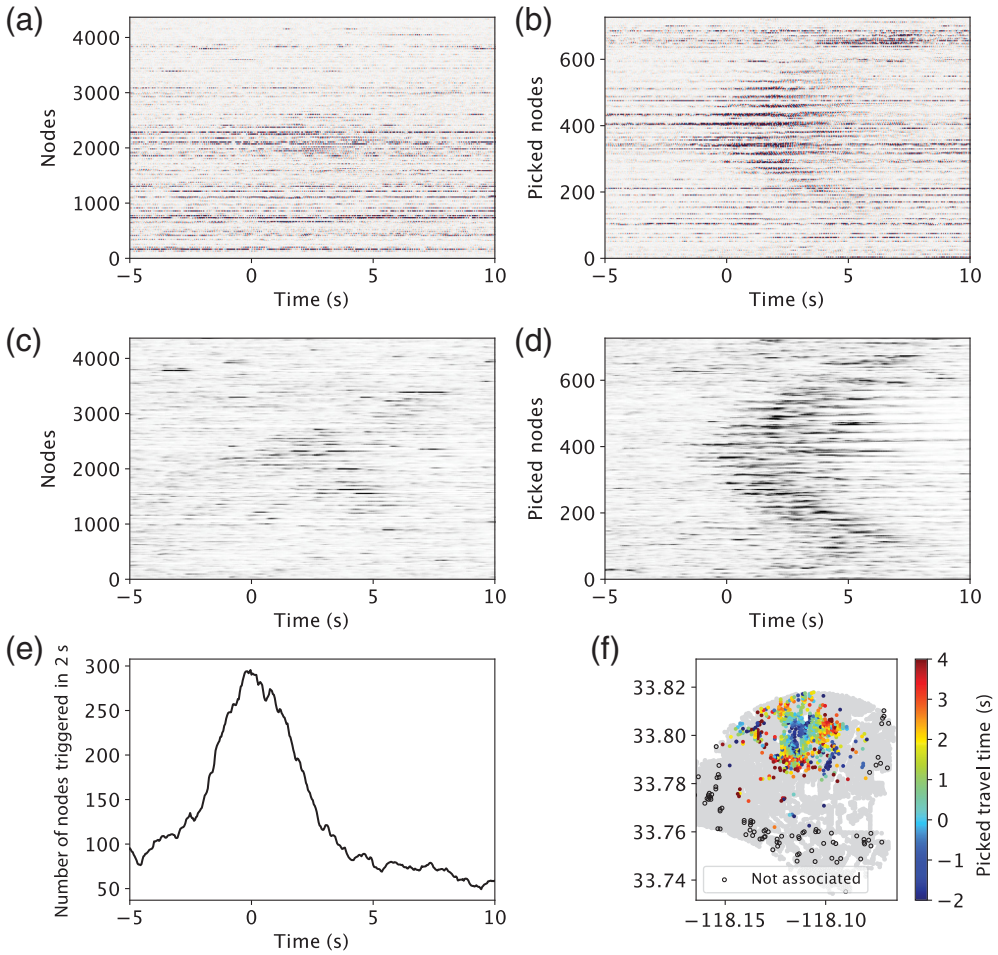

Figure 3. The scheme of detection and association. (a) The 15 s continuous waveforms around a detected event for all the sensors in SB3D array. (b) Similar to panel (a) but only for all the picked sensors. (c) Short-term average/long-term average (STA/LTA) of the data in panel (a). (d) Similar to panel (c) but only for all the picked sensors. (e) The number of the single-station picks in a 2 s sliding window for the picks in panel (c). The nodes plotted in (b) and (d) are picked based on the window with peak values. (f) The spatial distribution of all the picked sensors for this event, with colors showing the picked arrival times. Black circles represent the sensors that were picked during this event but did not pass the following spatial clustering for association.

months in the Long Beach area. The magnitudes of these events range between 0.40 and 1.34 with a mean value of 0.81. The distribution of the located seismicity is shown in Figure 5. The main feature of the seismicity is that the bulk of it is shallower than 2 km depth, with several large clusters along the NIF and around the Seal Beach Pier. Figure 5 shows two vertical cross sections of the located events, one of which has a high-resolution seismic reflection profile produced by 3D Seismic Solutions Inc shown in the background. The diffuse seismicity and the complicated seismic section show that at shallow depths, the NIF is a wide splay zone with a width >1 km. A new fault between the Los Alamitos fault (LAF) and the NIF and north of the Garden Grove fault (GGF) newly detected by oil company analysis is evident in the cross section (Fig. 5).

The hourly distribution of seismicity in all areas typically shows a bell-shaped distribution with a significant increase in the number of earthquakes at night due to the decrease in anthropogenic noise (Fig. 2). Although we only present nighttime events in this work, we also processed daytime data for comparison. Our results show that the number of events detected per hour in the nighttime is indeed higher than that in the daytime. The clusters of the events that appear during the daytime are mostly located around the Long Beach airport but do not appear to correspond to other areas of the city where we expect to have anthropological noise such as freeways and rail lines, industrial areas, port areas, and oil fields (Fig. S2). The calculated magnitudes for the daytime detections are substantially larger than that of nighttime events, which is due to the large amplitudes from the strong cultural noise right on the surface. The events' number-magnitude distribution also differs between the daytime and nighttime events (Fig. 6). We use the maximum curvature method to calculate the M_c (Wiemer and Wyss, 2000), in which M_c is set as the maximum of the first derivative of the discrete Gutenberg–Richter law plot. Then we use all the events above M_c to compute the b-value and its uncertainty with the maximum-likelihood estimate method (Aki, 1965). The daytime distribution is poorly fit with a power law, whereas the nighttime distribution has a regressed b-value of nearly 2 (Fig. 6). Currently, we do not include daytime detections in our results because we do not have a procedure for distinguishing between earthquake and anthropogenic noise sources.

Discussion

Active faults beneath Long Beach

The study area, comprising parts of Long Beach and Seal Beach, is crossed by the southern portion of the NIF, which appears on the U.S. Geological Survey (USGS) fault map to

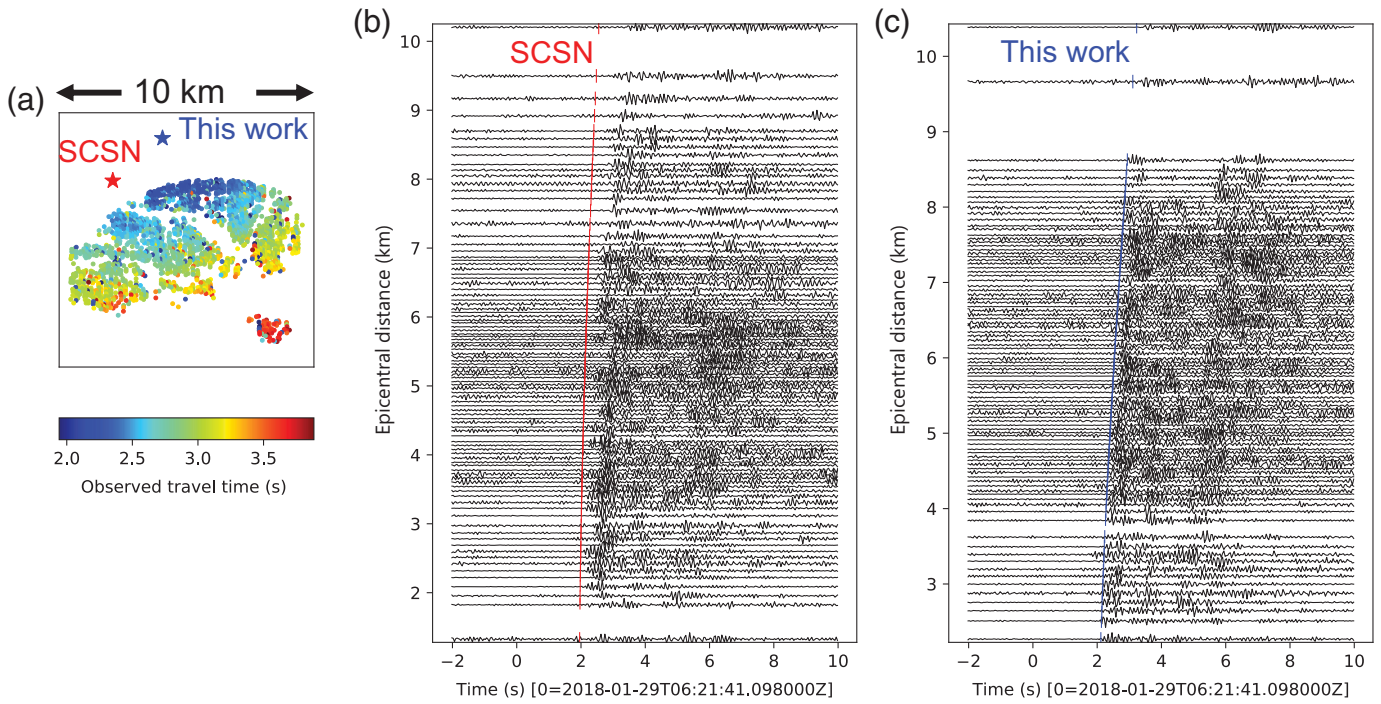

Figure 4. Comparison between the earthquake location in SCSN catalog and this study. (a) Epicenters of SCSN catalog in red and our located results in blue. The dots represent the sensors with color indicating the picked travel times. (b) Waveform sorted by the hypocenter in the red star in panel (a) with predicted *P*-wave arrival time shown in red bars. (c) Similar to panel (b) but for the hypocenter in blue in panel (a).

be a strike-slip fault with a single main strand. Detailed subsurface mapping of the oil fields along the NIF has revealed a variety of complex structural patterns, and many of these cannot easily be reconciled with a pure strike-slip origin (Wright, 1991). The formation of the splay features is likely related to the tectonic environment of the Los Angeles basin, in which the regional stress field transitioned from extension to compression (Harding, 1973; Williams *et al.*, 1989). Previous results support the idea that the NIF changes character along strike (Wright, 1991). In Long Beach, the NIF is a relatively simple fault with a pair of strands. In Seal Beach, the NIF is a wide flower structure with several splays currently active. Inbal *et al.* (2015) located the seismicity in Long Beach with the depths gradually increasing to the northeast of the NIF, indicating a dipping structure. The seismicity and the seismic reflection profile confirm that the NIF is dispersed across a zone that is at least 1 km wide at the surface (Fig. 5).

The active source portion of the Seal Beach array was processed by 3D Seismic Solutions Inc to produce 3D reflection images of the subsurface (Gish and Boljen, 2021). The top second of these images (~1 km in depth) is shown in Figure 5. Their analysis has identified a previously unknown fault with significant offset, in the area between the NIF and LAF faults, which they have named the GGF. At least part of the unmapped GGF is active, as shown in Figure 7. The seismicity pattern along the northwest–southwest trend is at a 10° angle to the shoreline as does the mapped fault. The seismicity ceases near the San Gabriel River where the fault is cut through by another orthogonal fault (Fig. 7). The southern end of both the fault and the seismicity is determined by the extent of the Seal Beach survey. The part of GGF without seismicity may be inactive during the very limited deployment duration. It is also possible that the events' frequency content is above the highest frequency used in this article.

Shallow seismicity

One notable feature is that most of the events detected in this study are clustered at very shallow depth (<2 km). Although the earthquakes in the SCSN catalog and the template-matching-based quake template matching catalog using regional stations (Ross *et al.*, 2019) are deeper than 6 km, previous studies using the Long Beach and extended Long Beach arrays present similar results showing the seismicity is clustered in the top 5 km (Li *et al.*, 2018; Yang *et al.*, 2021). We did not detect any deep events, but as shown by Inbal *et al.* (2016), detecting deep earthquakes in a noisy urban environment requires spatial filtering to reduce surface noise. Applying such a filter in this study would attenuate the detected shallow seismicity.

Tectonic seismicity in southern California is rarely observed shallower than 2 km (Sanders, 1990). A lack of near-source station coverage or the use of generalized regional velocity models has typically been considered as the cause of the large uncertainty in the earthquake depth in published catalogs. A sequence of unusually shallow earthquakes (<3 km) has been

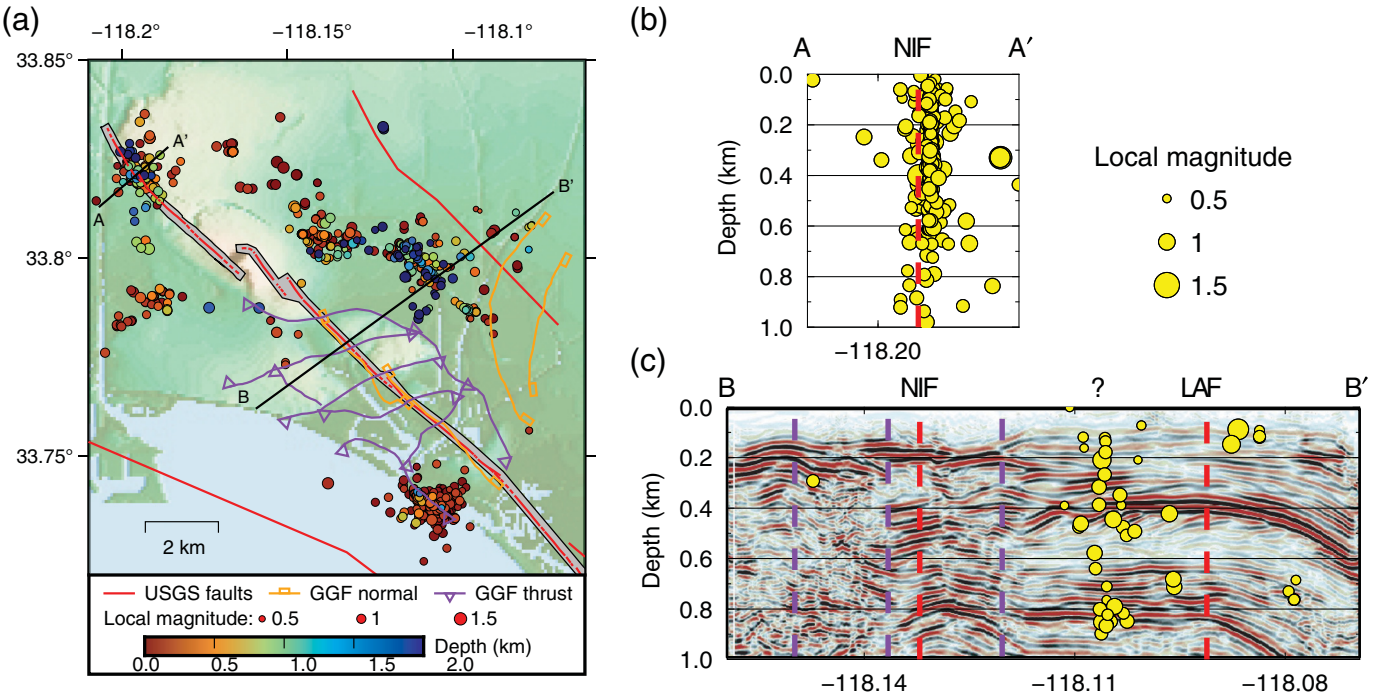

Figure 5. Distribution of the relocated nighttime events in the Long Beach area shown as circles. (a) The horizontal view. The circles are the events with their colors showing the depth and their sizes showing the magnitude. The red lines show the fault traces in USGS database (U.S. Geological Survey and California Geological Survey, 1993). The purple and the orange lines represent the recently mapped thrust and normal faults of the Garden Grove fault (GGF) zone, respectively (Gish and Boljen, 2021). The black lines mark the location of the two cross sections shown in panels (b) and (c). The gray shaded area depicts the ~250 m wide Alquist-Priolo zone as previously estimated (California Division of Mines and Geology [CDMG], 1976). (b) Seismicity on the depth profile AA′ with the red dashed line showing the location where the NIF crosses the profile. (c) Seismicity on the depth profile BB′ with the red dashed line showing the locations where the NIF and LAF cross the profile. The purple dashed lines show the locations where the GGF traces are across the profile. The background shows the high-resolution seismic reflection profile produced by 3DSeismicSolutions Inc. A question mark is placed above our located seismicity, indicating a possible unmapped fault in the region.

reported in 1993 inside the Rock Valley fault zone, Nevada (Smith *et al.*, 1993). The convincing evidence is the extremely short *S* minus *P* times recorded in their near-source three-component receiver. The nodal arrays in our study, however, only have single vertical component. We attempted to use the array data to determine focal mechanisms for identified earthquakes but were unsuccessful because spatial patterns were too noisy to be interpretable. We suspect this is due to paths being almost horizontal leaving the source (for shallow events) and hence encountering strong near-surface heterogeneity and scattering. An example is shown in Figure S3.

Relatively little is known about very shallow seismogenesis. Long (2019) summarizes the studies on shallow seismicity swarms in southeastern United States and proposes a positive feedback mechanism to account for the mechanics of shallow seismicity. The key is a low-stress environment rather than an increase in tectonic stress. In a low-stress environment, fractures can be open or filled with fluid and can be held open further by their asperities. During faulting, the reduction in fracture volume increases the fluid pressure, enhancing the capability of fluids to trigger more earthquakes. This mechanism works only at shallow depths and low stress where fractures and faults can hold fluids. In this fluid-rich environment, shallow seismicity may have different properties from the seismicity at greater depth. The focal mechanisms of shallow-induced seismicity are associated with joint directions (Zoback and Hickman, 1982), and the spectral decay of shallow seismicity is more rapid (Marion and Long, 1980). Many studies have also pointed that the shallow earthquakes generally have higher than normal *b*-values (Scholz, 1968; Mori and Abercrombie, 1997; Spada *et al.*, 2013; Li *et al.*, 2015; Goebel *et al.*, 2017; Meng *et al.*, 2018; Rivière *et al.*, 2018), which is consistent with the mechanism that they nucleate at lower differential stress (Scholz, 2015). A key question for hazard assessment is whether shallow seismicity increases seismic hazard. Although we expect that large earthquakes likely nucleate and release energy at 6–10 km depth, shallow seismicity suggests that there are many possible paths for a rupture to propagate to the surface. The regulatory zones surrounding the surface traces of active faults in California are called the Alquist-Priolo zone, which has a minimum extent of 50 ft from the fault. Our results suggest that the zone of high hazard at the surface may therefore be much wider than the Alquist-Priolo zone indicates (Fig. 5).

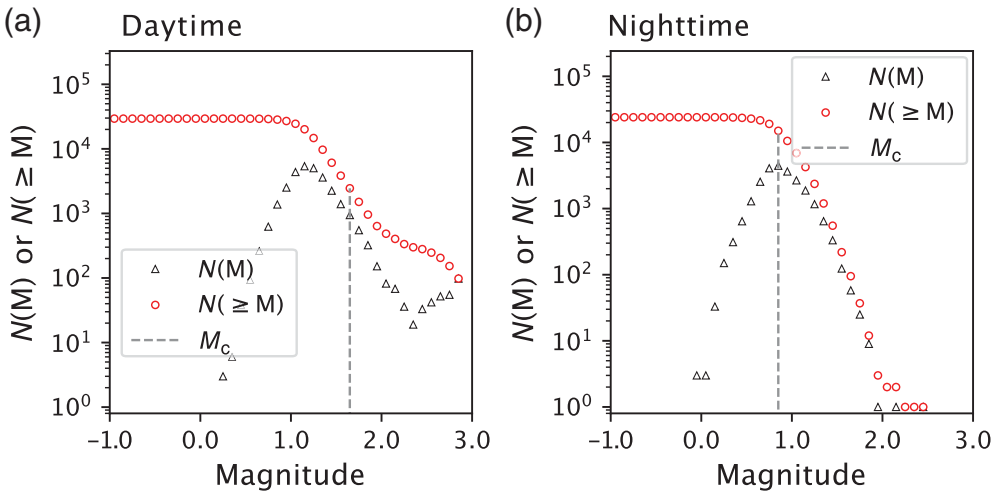

Figure 6. Magnitude distribution for daytime and nighttime events. (a) Magnitude distribution for daytime events. (b) Magnitude distribution for nighttime events. Here, all the events, including those that were not relocated, are plotted. The nighttime distribution is more consistent with a power law whereas the daytime events clearly do not follow a power law.

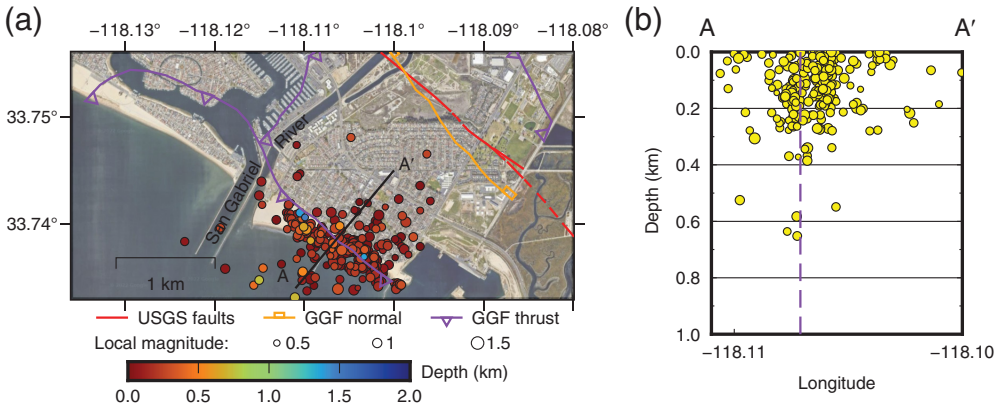

Figure 7. A zoomed-in view of the cluster of shallow seismicity in the southeast corner of the study region. (a) The seismicity identifies a fault along the coast that is also identified in the interpretation of the seismic data by the company 3DSeismicSolutions. This fault is intersected or truncated on the northwest by another fault. Note that this seismicity is ~2–3 km away from the Seal Beach oilfield. The symbols of the faults are the same as those in Figure 5. (b) Seismicity along the depth profile AA′. The magnitude scale is the same as that in panel (a). The purple dashed line shows the location where the fault mapped by reflection surveys intersects with the profile.

Conclusions

We use three dense urban exploration seismic networks in Long Beach, California, to detect and locate local seismicity. Besides the documented events from outside the arrays in SCSN catalog, many shallow events inside the array are detected. The location results support the previous conclusion that the NIF is a wide splayed fault in this area. The seismicity pattern also compares well with some newly identified faults from reflection seismic surveys. The shallow events call for attention on the potential shallow seismicity-related hazard.

Data and Resources

The supplemental material for this article contains the following: Figure S1 shows our attempt to use a machine learning–based denoiser before seismicity detection. Figure S2 shows the detected and located daytime events. Figure S3 shows our attempt to determine the focal mechanism of the detected small events. The seismic data used in this study were recorded as part of three exploration surveys. The two surveys in the Long Beach area are property of Signal Hill Petroleum LLC, and permission to use the data must be obtained from them. The survey in the Seal Beach area is managed by 3D Seismic Solutions, and permission to use may be obtained from that company. The seismic catalog produced by this study is available at https://data.caltech.edu/records/5ws5e-ddh43. The fault locations in Figure 1 are publicly available at https://www.usgs.gov/natural-hazards/earthquake-hazards/faults. The software used in this study are publicly available and downloaded from NonLinLoc (https://github.com/alomax/NonLinLoc) and GrowClust (https://github.com/dttrugman/GrowClust). All websites were last accessed in March 2023.

Declaration of Competing Interests

The authors acknowledge that there are no conflicts of interest recorded.

Acknowledgments

The authors thank Signal Hill Petroleum for providing access to the two Long Beach surveys and 3D Seismic Solutions for access to the Seal Beach survey. Dan Hollis and Eric Campbell were key to providing this access. The authors thank Dan Gish and Steve Boljen of 3D Seismic Solutions for providing the seismic cross section and the locations of the faults shown in Figure 5. The authors thank Susan Hough for helpful comments in the article. The authors thank Daniel Trugman and an anonymous reviewer for their insightful comments and advice. This study was supported by the Southern California

Earthquake Center (SCEC) Award Number 21034. Part of the material presented in this article was reported as a progress report to SCEC as part of the results of an SCEC award.

References

Aki, K. (1965). Maximum likelihood estimate of b in the formula logN=a-bM and its confidence limits, *Bull. Earthq. Res. Inst. Univ. Tokyo* **43,** 237–239.

Bungum, H., E. S. Husebye, and F. Ringdal (1971). The NORSAR array and preliminary results of data analysis, *Geophys. J. Int.* **25,** nos. 1/3, 115–126, doi: 10.1111/j.1365-246X.1971.tb02334.x.

California Division of Mines and Geology (CDMG) (1976). Active fault mapping and evaluation program—Ten year program to implement Alquist-Priolo special studies zones act, California division of mines and geology special publication, *California Division of Mines and Geology Special Publication*, available at https://www.conservation.ca.gov/cgs/alquist-priolo (last accessed March 2023).

Castellanos, J. C., R. W. Clayton, and A. Juarez (2020). Using a time-based subarray method to extract and invert noise-derived body waves at long beach, California, *J. Geophys. Res.* **125,** no. 5, doi: 10.1029/2019JB018855.

Eaton, J. E. (1933). Long beach, California, earthquake of March 10, 1933: Geological notes, *AAPG Bull.* **17,** no. 6, 732–738, doi: 10.1306/3D932B6C-16B1-11D7-8645000102C1865D.

Field, E. H., G. P. Biasi, P. Bird, T. E. Dawson, K. R. Felzer, D. D. Jackson, K. M. Johnson, T. H. Jordan, C. Madden, A. J. Michael, *et al.* (2015). Long-term time-dependent probabilities for the third uniform California earthquake Rupture Forecast (UCERF3), *Bull. Seismol. Soc. Am.* **105,** no. 2A, 511–543, doi: 10.1785/0120140093.

Gish, D., and S. Boljen (2021). Newly identified fault in Seal Beach, CA, quietly rattles beneath the city, *Temblor* doi: 10.32858/temblor.219.

Goebel, T. H. W., G. Kwiatek, T. W. Becker, E. E. Brodsky, and G. Dresen (2017). What allows seismic events to grow big?: Insights from b-value and fault roughness analysis in laboratory stick-slip experiments, *Geology* **45,** no. 9, 815–818, doi: 10.1130/G39147.1.

Harding, T. P. (1973). Newport-Inglewood trend, California—An example of wrenching style of deformation, *AAPG Bull.* **57,** 97–116, doi: 10.1306/819A424C-16C5-11D7-8645000102C1865D.

Hauksson, E. (1987). Seismotectonics of the Newport-Inglewood fault zone in the Los Angeles basin, southern California, *Bull. Seismol. Soc. Am.* **77,** no. 2, 539–561.

Hauksson, E., and S. Gross (1991). Source parameters of the 1933 Long Beach earthquake, *Bull. Seismol. Soc. Am.* **81,** no. 1, 81–98.

Hough, S. E., and R. W. Graves (2020). The 1933 Long Beach Earthquake (California, USA): Ground motions and rupture scenario, *Sci. Rep.* **10,** no. 1, 10017, doi: 10.1038/s41598-020-66299-w.

Hutton, K., J. Woessner, and E. Hauksson (2010). Earthquake monitoring in Southern California for seventy-seven years (1932-2008), *Bull. Seismol. Soc. Am.* **100,** no. 2, 423–446, doi: 10.1785/0120090130.

Inbal, A., J.-P. Ampuero, and R. W. Clayton (2016). Localized seismic deformation in the upper mantle revealed by dense seismic arrays, *Science* **354,** no. 6308, 88–92, doi: 10.1126/science.aaf1370.

Inbal, A., R. W. Clayton, and J.-P. Ampuero (2015). Imaging widespread seismicity at midlower crustal depths beneath Long Beach, CA, with a dense seismic array: Evidence for a depth-dependent earthquake size distribution, *Geophys. Res. Lett.* **42,** no. 15, 6314–6323, doi: 10.1002/2015GL064942.

Li, Z., Z. Peng, D. Hollis, L. Zhu, and J. McClellan (2018). High-resolution seismic event detection using local similarity for Large-N arrays, *Sci. Rep.* **8,** no. 1, 1–10, doi: 10.1038/s41598-018-19728-w.

Li, Z., Z. Peng, X. Meng, A. Inbal, Y. Xie, D. Hollis, and J. P. Ampuero (2015). Matched filter detection of microseismicity in long beach with a 5200-station dense array, *SEG Technical Program Expanded Abstracts 34*, 2615–2619, doi: 10.1190/segam2015-5924260.1.

Lin, F. C., D. Li, R. W. Clayton, and D. Hollis (2013). High-resolution 3D shallow crustal structure in Long Beach, California: Application of ambient noise tomography on a dense seismic array, *Geophysics* **78,** no. 4, doi: 10.1190/geo2012-0453.1.

Lomax, A., A. Michelini, and A. Curtis (2014). Earthquake location, direct, global-search methods, in *Encyclopedia of Complexity and Systems Science*, R. Meyers (Editor), Springer, New York, New York, 1–33, doi: 10.1007/978-3-642-27737-5_150-2.

Lomax, A., J. Virieux, P. Volant, and C. Berge-Thierry (2000). Probabilistic earthquake location in 3D and layered models, in *Advances in Seismic Event Location. Modern Approaches in Geophysics*, C. H. Thurber and N. Rabinowitz (Editors), Vol. 18, Springer, Dordrecht, The Netherlands, doi: 10.1007/978-94-015-9536-0_5.

Long, L. T. (2019). The mechanics of natural and induced shallow seismicity: A review and speculation based on studies of eastern U.S. Earthquakes, *Bull. Seismol. Soc. Am.* **109,** no. 1, 336–347, doi: 10.1785/0120180134.

Marion, G. E., and L. T. Long (1980). Microearthquake spectra in the southeastern United States, *Bull. Seismol. Soc. Am.* **70,** no. 4, 1037–1054, doi: 10.1785/BSSA0700041037.

Meng, X., H. Yang, and Z. Peng (2018). Foreshocks, b value map, and aftershock triggering for the 2011 Mw 5.7 Virginia Earthquake, *J. Geophys. Res.* **123,** no. 6, 5082–5098, doi: 10.1029/2017JB015136.

Mori, J., and R. E. Abercrombie (1997). Depth dependence of earthquake frequency-magnitude distributions in California: Implications for rupture initiation, *J. Geophys. Res.* **102,** no. B7, 15,081–15,090, doi: 10.1029/97jb01356.

Mousavi, S. M., W. L. Ellsworth, W. Zhu, L. Y. Chuang, and G. C. Beroza (2020). Earthquake transformer—An attentive deep-learning model for simultaneous earthquake detection and phase picking, *Nat. Commun.* **11,** no. 1, 1–12, doi: 10.1038/s41467-020-17591-w.

Richter, C. F. (1935). An instrumental earthquake magnitude scale, *Bull. Seismol. Soc. Am.* **25,** no. 1, 1–32, doi: 10.1785/BSSA0250010001.

Rivière, J., Z. Lv, P. A. Johnson, and C. Marone (2018). Evolution of b-value during the seismic cycle: Insights from laboratory experiments on simulated faults, *Earth Planet. Sci. Lett.* **482,** 407–413, doi: 10.1016/j.epsl.2017.11.036.

Ross, Z. E., M. A. Meier, E. Hauksson, and T. H. Heaton (2018). Generalized seismic phase detection with deep learning, *Bull. Seismol. Soc. Am.* **108,** no. 5, 2894–2901, doi: 10.1785/0120180080.

Ross, Z. E., D. T. Trugman, E. Hauksson, and P. M. Shearer (2019). Searching for hidden earthquakes in Southern California, *Science* **771,** 767–771, doi: 10.1126/science.aaw6888.

Sanders, C. O. (1990). Earthquake depths and the relation to strain accumulation and stress near strike-slip faults in southern

California, *J. Geophys. Res.* **95,** no. B4, 4751–4762, doi: 10.1029/JB095iB04p04751.

Scholz, C. H. (1968). The frequency-magnitude relation of microfracturing in rock and its relation to earthquakes, *Bull. Seismol. Soc. Am.* **58,** no. 1, 399–415, doi: 10.1785/BSSA0580010399.

Scholz, C. H. (2015). On the stress dependence of the earthquake b value, *Geophys. Res. Lett.* **42,** no. 5, 1399–1402, doi: 10.1002/2014GL062863.

Shelly, D. R., G. C. Beroza, and S. Ide (2007). Non-volcanic tremor and low-frequency earthquake swarms, *Nature* **446,** no. 7133, 305–307, doi: 10.1038/nature05666.

Small, P., D. Gill, P. J. Maechling, R. Taborda, S. Callaghan, T. H. Jordan, K. B. Olsen, G. P. Ely, and C. Goulet (2017). The SCEC unified community velocity model software framework, *Seismol. Res. Lett.* **88,** no. 6, 1539–1552, doi: 10.1785/0220170082.

Smith, K., G. Shields, and J. Brune (1993). Shallow earthquakes, rock valley fault zone, Southern Nevada test site 1 a sequence of very shallow earthquakes in the rock valley Fault Zone, Southern Nevada test site, *Eos Suppl.* **74,** 417.

Snover, D., C. W. Johnson, M. J. Bianco, and P. Gerstoft (2020). Deep clustering to identify sources of urban seismic noise in long beach, California, *Seismol. Res. Lett.* doi: 10.1785/0220200164.

Spada, M., T. Tormann, S. Wiemer, and B. Enescu (2013). Generic dependence of the frequency-size distribution of earthquakes on depth and its relation to the strength profile of the crust, *Geophys. Res. Lett.* **40,** no. 4, 709–714, doi: 10.1029/2012GL054198.

Taber, S. (1920). The Inglewood earthquake in Southern California, June 21, 1920, *Bull. Seismol. Soc. Am.* **10,** no. 3, 129–145, doi: 10.1785/BSSA0100030129.

Trugman, D. T., and P. M. Shearer (2017). GrowClust: A Hierarchical clustering algorithm for relative earthquake relocation, with application to the Spanish Springs and Sheldon, Nevada, earthquake sequences, *Seismol. Res. Lett.* **88,** no. 2, 379–391, doi: 10.1785/0220160188.

U.S. Geological Survey and California Geological Survey (1993). *Quaternary fault and fold database for the United States*, available at https://www.usgs.gov/programs/earthquake-hazards/faults (last accessed March 2023).

White, M. C. A., Y. Ben-Zion, and F. L. Vernon (2019). A detailed earthquake catalog for the San Jacinto fault-zone region in southern California, *J. Geophys. Res.* **124,** no. 7, 6908–6930, doi: 10.1029/2019JB017641.

Wiemer, S., and M. Wyss (2000). Minimum magnitude of completeness in earthquake catalogs: Examples from Alaska, the Western United States, and Japan, *Bull. Seismol. Soc. Am.* **90,** no. 4, 859–869, doi: 10.1785/0119990114.

Williams, G. D., C. M. Powell, and M. A. Cooper (1989). Geometry and kinematics of inversion tectonics, *Geol. Soc. Lond. Spec. Publ.* **44,** no. 1, 3–15, doi: 10.1144/GSL.SP.1989.044.01.02.

Withers, M., R. Aster, C. Young, J. Beiriger, M. Harris, S. Moore, and J. Trujillo (1998). A comparison of select trigger algorithms for automated global seismic phase and event detection, *Bull. Seismol. Soc. Am.* **88,** no. 1, 95–106.

Wood, H. O., J. P. Buwalda, and R. R. Martel (1933). The long beach earthquake, *Science* **78,** no. 2016, 147–149.

Wright, T. L. (1991). Structural geology and tectonic evolution of the Los Angeles Basin, California, *Act. Margin Basins* 35–134.

Yang, L., X. Liu, and G. C. Beroza (2021). Revisiting evidence for widespread seismicity in the upper mantle under Los Angeles, *Sci. Adv.* **7,** no. 4, doi: 10.1126/sciadv.abf2862.

Yang, L., X. Liu, W. Zhu, L. Zhao, and G. C. Beroza (2022). Toward improved urban earthquake monitoring through deep-learning-based noise suppression, *Sci. Adv.* **8,** no. 15, eabl3564, doi: 10.1126/sciadv.abl3564.

Zhu, W., and G. C. Beroza (2019). PhaseNet: A deep-neural-network-based seismic arrival-time picking method, *Geophys. J. Int.* **216,** no. 1, 261–273, doi: 10.1093/gji/ggy423.

Zoback, M. D., and S. Hickman (1982). In situ study of the physical mechanisms controlling induced seismicity at Monticello Reservoir, South Carolina, *J. Geophys. Res.* **87,** no. B8, 6959–6974, doi: 10.1029/JB087iB08p06959.

Manuscript received 7 November 2022
Published online 5 April 2023